

Near-field thermal transport in a nanotip under laser irradiation

This article has been downloaded from IOPscience. Please scroll down to see the full text article.

2011 Nanotechnology 22 075204

(<http://iopscience.iop.org/0957-4484/22/7/075204>)

View [the table of contents for this issue](#), or go to the [journal homepage](#) for more

Download details:

IP Address: 129.186.209.60

The article was downloaded on 16/02/2011 at 16:05

Please note that [terms and conditions apply](#).

Near-field thermal transport in a nanotip under laser irradiation

Xiangwen Chen and Xinwei Wang¹

Department of Mechanical Engineering, 2010 Black Engineering Building, Iowa State University, Ames, IA 50011, USA

E-mail: xwang3@iastate.edu

Received 10 September 2010, in final form 17 December 2010

Published 14 January 2011

Online at stacks.iop.org/Nano/22/075204

Abstract

We report on a systematic study of highly enhanced optical field and its induced thermal transport in nanotips under laser irradiation. The effects on electric field distribution caused by curvature radius, tip aspect ratio, and polarization angle of the incident laser are studied. Our Poynting vectors' study clearly shows that when a laser interacts with a metal tip, it is bent around the tip and concentrated under the apex, where extremely high field enhancement appears. This phenomenon is more like a liquid flow being forced/squeezed to go through a narrow channel. As the tip–substrate distance increases, the peak field enhancement decreases exponentially. A shift of field peak position away from the tip axis is observed. For the incident light, only its component along the tip axis direction has a contribution to the electric field enhancement under the tip apex. The optimum tip apex radius for field enhancement is about 9 nm when the half taper angle is 10°. For a tip with a fixed radius of 30 nm, field enhancement increases with the half taper angle when it is less than 25°. The thermal transport inside the nanoscale tungsten tips due to absorption of incident laser light is explored using the finite element method. A small fraction of light penetrates into the tip. As the polarization angle or apex radius increases, the peak apex temperature decreases. The peak apex temperature goes down as the half taper angle increases, even though the mean laser intensity inside the tip increases, revealing a very strong effect of the taper angle on thermal transport.

(Some figures in this article are in colour only in the electronic version)

1. Introduction

In recent decades, the interaction of a scanning probe microscope (SPM) tip with an external illuminating laser has motivated considerable new exciting developments. The introduction of near-field scanning optical microscopy (NSOM/SNOM) [1, 2]—a distinct imaging method based on near-field enhancement at coated, pulled capillaries—has extended the optical microscopy technology beyond the diffraction limit that constrains the resolution to no finer than $\sim\lambda/2$ (λ : light wavelength). Later, apertureless NSOM was realized [3], and has stimulated much interest in this area [4–7]. The circumvention of the optical diffraction limit made it feasible for near-field laser-assisted SPM-based nanoprocessing [8–13], which offers the capacity of producing surface features as small as 10–50 nm [14]. Combined

with the near-field technique, surface enhanced Raman scattering (SERS) [15–18] and tip enhanced Raman scattering (TERS) [19–22] have proved promising and powerful tools for material analyzing at nanoscale. The term TER came into use after 2000 following the pioneering TERS-related work in the 1990s [23–25],

The phenomenon of optical field enhancement has been theoretically reported over the years. An analytical solution for a sphere under laser illumination has been developed by using the Mie scattering theory [26]. To solve the electromagnetic field distribution for a specific geometry, many methods have been used. Examples of such methods include the multiple multipole method (MMP) [7, 20, 27], the Green's function method [28], the method of moment [29], the boundary element method [22, 30], the generalized field propagator technique [31, 32], and the finite difference in time domain (FDTD) method [10, 11, 21, 33–36]. The finite element method (FEM) is another important one that

¹ Author to whom any correspondence should be addressed.

has become more and more popular and is user-friendly and commercially available. The FEM has proved fruitful for solving electromagnetic problems especially for tip–substrate systems [21, 37–42].

Another aspect of interest is the temperature in the tip due to the laser induced heating. The temperature profiles along the aluminum-coated fiber tip due to local heating were calculated or measured by several groups in the mid-1990s [43–48]. The heating was shown to be strongly dependent on the taper angle of the tip: decreasing with increasing taper angle [44, 48]. The temperature coefficients varied from $20 \text{ K m}^{-1} \text{ W}^{-1}$ for a tip with large cone angle to $60 \text{ K m}^{-1} \text{ W}^{-1}$ for the narrow one [44]. The measured temperature increase at a distance of $70 \mu\text{m}$ from the aperture (apex) was linear with the input light power until the coating was damaged [43, 44]. The probe could be damaged as a result of thermal stress caused by different thermal expansions of the fiber and aluminum coating [43–48]. La Rosa also measured the two-time-constant tip expansion in later work [49]. Miskovsky *et al* [50] solved the heat conduction equation by using the Green function formalism and got the transient temperature distribution for axial symmetric illumination of the tip. The temperature in the tungsten tip can rise by about 100° [37, 50]. A maximal tip temperature as high as 650 K was also reported by Ukraintsev and Yates [51]. Thermal response and thermal expansion were usually coupled in tip–substrate systems [37, 51–54]. Gerstner *et al* [37] investigated the temperature distribution along the tip axis and thermal expansion of a scanning tunneling microscope (STM) tip by the FEM. The calculation indicated that the tip bending due to asymmetric laser heating was of the same order as thermal expansion. The temperature distribution in tungsten was also calculated by the boundary element method (BEM) [55]. The temperature in a thin and semi-infinite metallic sample was also compared [55, 56]. The calculations showed that the maximal temperature of the thin metallic film is one order of magnitude larger than for the thick sample [56]. Geshev *et al* [57] developed a mathematical model for the temperature of an STM tip, based on the averaged one-dimensional heat conduction equation. In this model, the tip is heated by two parts: enhanced field incident on the tip and a laser light spot focused on the lateral tip boundary. The latter is the main contribution to the thermal expansion of the tungsten STM tip. McCarthy *et al* [58] designed an experimental procedure, based on Raman scattering, for measuring the apex temperature of a laser heated probe tip, and presented a closed-form analytical expression that accurately modeled the heating process. Other temperature increase models also have been brought forward by Mai *et al* [59] and Grigoropoulos and co-workers [11]. Downes *et al* [34] calculated the temperature distribution in the tip–substrate system for a variety of tip and substrate materials, and for air and aqueous environments under steady state conditions. Recently, Milner *et al* [60] demonstrated a method to determine the tip temperature under laser illumination by observing the shift of the silicon Raman line scattered from the tip and by monitoring the mechanical resonance frequency shift of the probe.

In this work, a high-fidelity and full field study is conducted to study the thermal evolution and thermal

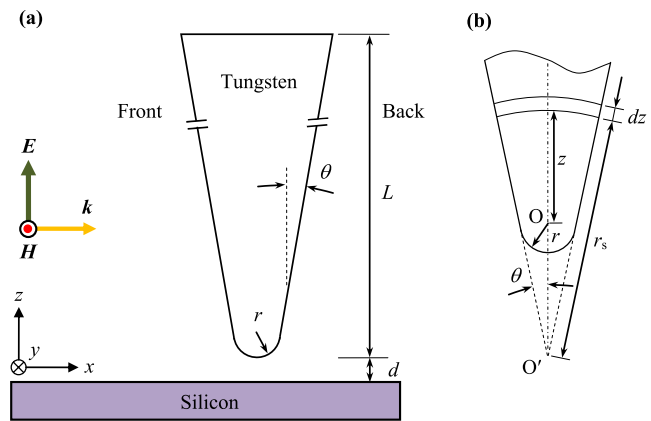


Figure 1. (a) Schematic of the tip–substrate system studied in this work, (b) geometric structure of the tip.

distribution in an SPM tip under laser irradiation. The electric field distribution and enhancement is calculated in the tip–substrate system by using the FEM. The dependence of field distribution around the tip and within the tip on incident laser polarization direction, tip–substrate distance, tip apex radius, and tip half taper angle are studied systematically. According to the electric field distribution within the tip, which would act as a heating source to heat up the tip, the temperature distribution inside the tip is calculated. The influence of geometric factors on the temperature distribution is also reported.

2. Basics of modeling

The modeling is performed by using a high-frequency structure simulator (HFSS V12.1 Ansoft, Inc.), a full-wave high-frequency 3D finite element modeler of Maxwell's equations. A conical tungsten tip whose sharp end is tangential to a hemisphere and silicon substrate system, as shown in figure 1(a), is investigated in this work. Maxwell's equations are solved across a defined rectangular computational domain with dimensions L_x (650–1500 nm), L_y (650–1500 nm), L_z (550–3000 nm) containing the tip, substrate, and vacuum filled surroundings. Absorbing (radiation) boundaries, which balloon the boundaries infinitely far away from the structure, is applied for the domain. The whole domain is split into tetrahedral elements with their length less than $\lambda/4$ (λ : laser wavelength). The mesh is adaptively refined where high field gradient occurs during simulation.

A plane wave is incident horizontally from the front side (along the x direction) of the model; and the electric field amplitude of the wave is set to 1 V m^{-1} . Thus, the electric field amplitude of the scattered light is equal to the field enhancement value, which is defined as the ratio of scattered to incident field amplitude. The polarization direction has an angle ϕ with respect to the z -axis. For most situations, $\phi = 0^\circ$, as shown in figure 1(a), except for studying the polarization effects of incident light. The wavelength of incident light is 532 nm . At the corresponding frequency, the permittivities of tungsten and silicon are, $\epsilon = 4.71 + 18.93i$ and $\epsilon =$

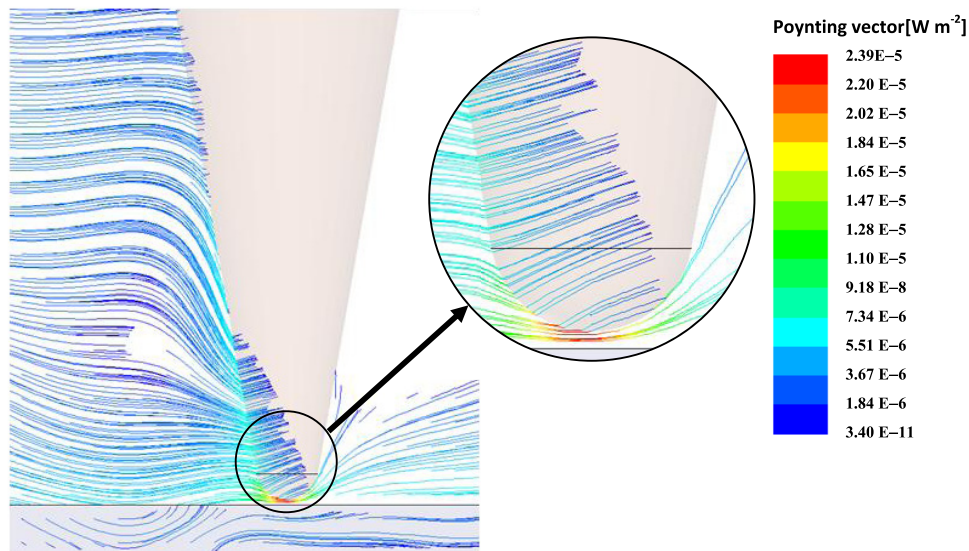


Figure 2. Streamlines of Poynting vectors in the x - z plane (laser is incident from the left side). In a propagating sinusoidal electromagnetic plane wave of a fixed frequency, the Poynting vector, presenting the energy flux (in W m^{-2}), always points to the direction of energy propagation. Simulation configuration: $d = 5$ nm, $r = 30$ nm, $\theta = 10^\circ$ and $\phi = 0^\circ$.

$17.24 + 0.024i$, respectively [61]. The electric conductivities of tungsten and silicon are $5.93 \times 10^5 \text{ S m}^{-1}$ and $1.34 \times 10^5 \text{ S m}^{-1}$, respectively. The real part of the permittivity of tungsten is positive (the frequency used in the simulation is larger than the plasma frequency ω_p), therefore the surface of the tip does not support a propagating surface plasmon. On the other hand, the field enhancement still appears because of the resonant tip-substrate system, but is much less than that for Ag or Au tips at the same frequency.

The tip shape is described by three parameters: half taper angle θ , apex radius r , and length L (as shown in figure 1(a)). The electric field distribution in the tip-substrate system has been calculated for a range of tip lengths (300–2400 nm), and the results show that the field distribution in the system remains constant in the tip length range (less than 10% difference), which is akin to the conclusion reached by FDTD simulation for $L > \lambda$ [35, 62]. Consequently, the length of tips in all models is set as 600 nm, which is a good approximation for commercial tips as long as $15 \mu\text{m}$. Different half taper angles and apex radii are chosen to investigate the geometric effects on the electric field enhancement, or intensity enhancement that is defined as the squared ratio of scattered to incident field amplitudes multiplied by the ratio of refractive indices of the media. Simulations have been performed on a platform consisting of a 2.53 GHz Core 2 Duo Processor of Intel with 4 GB RAM.

3. Optical field distribution within and outside the tip

3.1. Optical field distribution

In order to observe how the electromagnetic wave propagates in the tip-substrate system, the streamlines of Poynting vectors are shown in the x - z cross-section in figure 2. In electromagnetic waves, the energy flow is described by the Poynting vector $\mathbf{S} = \mathbf{E} \times \mathbf{H}$, where $\mathbf{E}(\mathbf{H})$ represents the

electric (magnetic) field. In this case, the light is incident along the $+x$ direction, and the polarization direction is parallel to the z -axis. The tip is perpendicularly located 5 nm above the silicon substrate. In a propagating sinusoidal electromagnetic plane wave of a fixed frequency, the Poynting vector, presenting the energy flux (in W m^{-2}), oscillates and always points to the direction of energy propagation. As a result, the streamline of Poynting vectors can give some information about the wave factors \mathbf{k} , or the propagation of the laser beam. When the electromagnetic wave is far away from the tip, the propagation direction is not affected by it, almost perpendicular to the tip axis. When an electromagnetic wave interacts with the conical metal tip, the direction of the electromagnetic wave redirects according to the geometric surface. The direction of the propagation converges toward the tip apex, and through the gap between the tip and substrate. The laser acts more like fluid, and the tip-substrate like a throttling set. The electromagnetic wave is squeezed in the vicinity of the tip apex. Furthermore, higher energy flow appears in this area as the red streamline shows in figure 2. While most of the electromagnetic wave detours around the tip apex to get through the metal barrier, nevertheless, a small portion of the electromagnetic wave plunges into the metal tip, and propagates in the tip following the attenuating rule. That is the reason why the phenomenon of electric field enhancement happens under the tip apex. Also when the electromagnetic field enters the tip, it will bend up a little bit rather than propagate in the x direction due to refraction.

Figure 3 shows how the electric field is distributed in the tip-substrate system. From figures 3(a) and (b), it is noticed that a strong electric field gradient occurs in the tip-substrate gap; and resonance happens here. The highest field enhancement factor (in this paper, all field enhancement below refers to the highest field enhancement factor) as high as 15 appears normally beneath the tip apex. Symmetric electric

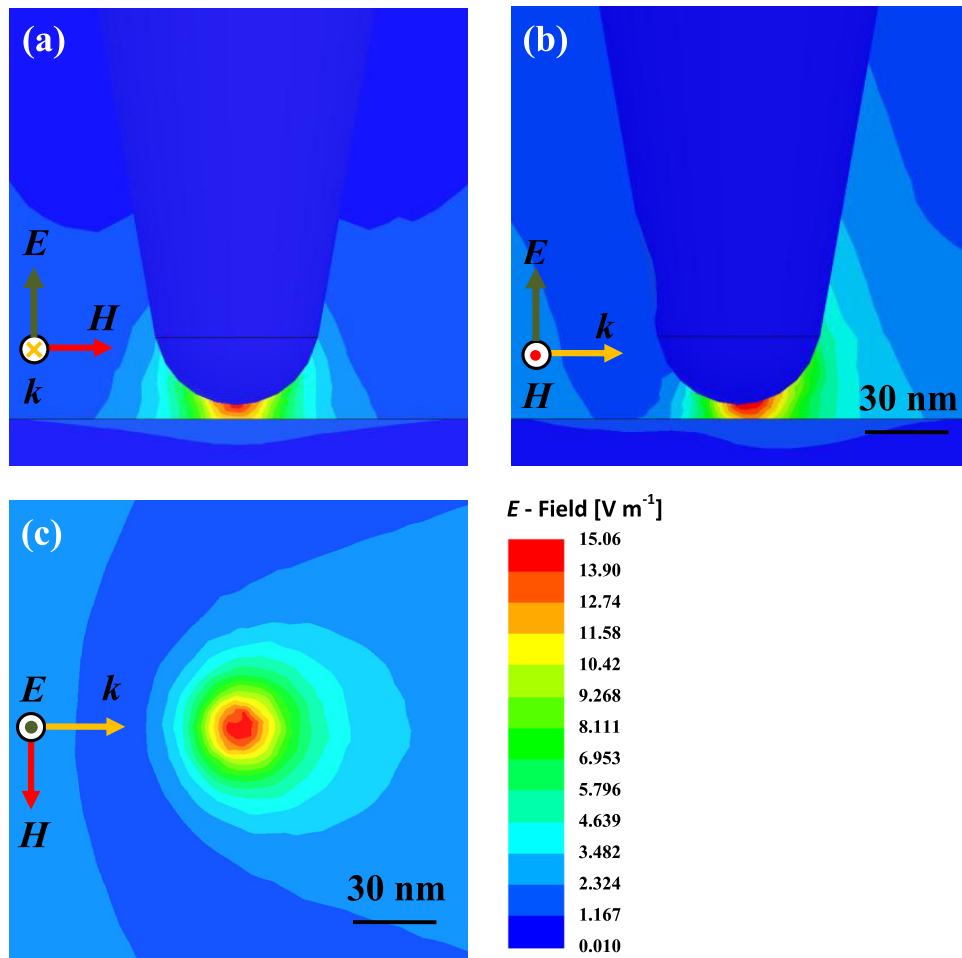


Figure 3. Electric field distribution around the tip apex for (a) the front view in the y - z plane and (b) the side view in the x - z plane, and (c) the top view of the cross-section under the tip apex. The simulation conditions are the same as those for figure 2.

field distribution is observed from the front, as in figure 3(a). However, the side view (in figure 3(b)) has a different story: the electric field gradient on the front (upwind) side is stronger than on the back (downwind) side, and the gradient line contour of electric field seems to be blown away along the laser incident direction. The same conclusion is also drawn from the top view in figure 3(c): the contour is dense on the front side and sparse on the back side. As regard to the electric field inside the tip, compared to that in the gap zone, it is quite low, for the small amount of laser that propagates into the metal would be absorbed promptly along the propagation direction. On the other hand, the laser beam has plunged into in the silicon substrate within a small zone beneath the tip, which is the source of the Raman signal.

In the next step, we study the electric field distribution inside the tip, as shown in figure 4. Observed from the upper part of the tip in figures 4(a) and (b), the electromagnetic field impinges into the metal tip from all directions, and then is attenuated toward the tip core. As expected, the electric field inside the tip on the front (upwind) side is much stronger than that on the back (downwind) side, as shown in figure 4(b). In figure 4(c), the electric field amplitude drops exponentially as the electromagnetic wave transmits into the core of the tip. As the amplitude drops to e^{-1} of that on the surface,

the length from the surface to P is called the skin depth δ , which is 36.5 nm, a little larger than the theoretical value of 31.1 nm ($\delta = \lambda/2\pi k$). Considering that the electromagnetic wave inside the tip is the superposition of the electromagnetic wave transmitted from all surrounding directions rather than only from the $-x$ direction, the appearance of position P is postponed toward the core of the tip. Meanwhile, the bending up of the electromagnetic wave direction after it enters the tip surface as shown in figure 2 is also a reason why the skin depth calculated in the x direction is larger than the theoretical value. Examining the electric field distribution in the sharp part of the tip in figure 4(b), we find the strongest electric field is as high as 1.01 V m^{-1} , even stronger than that of the incident laser. However, this does not violate the optical law, for the amplitude outside the tip is much higher than the input laser, no wonder the amplitude inside is higher than 1 V m^{-1} .

3.2. Laser polarization direction

The field enhancement depends strongly on the incident field polarization. Novotny *et al* have shown that the electrical field component along the tip axis gives rise to the field enhancement [27, 63]; Martin and Girard concluded that the vertical field component plays a dominating role [31]. Similar

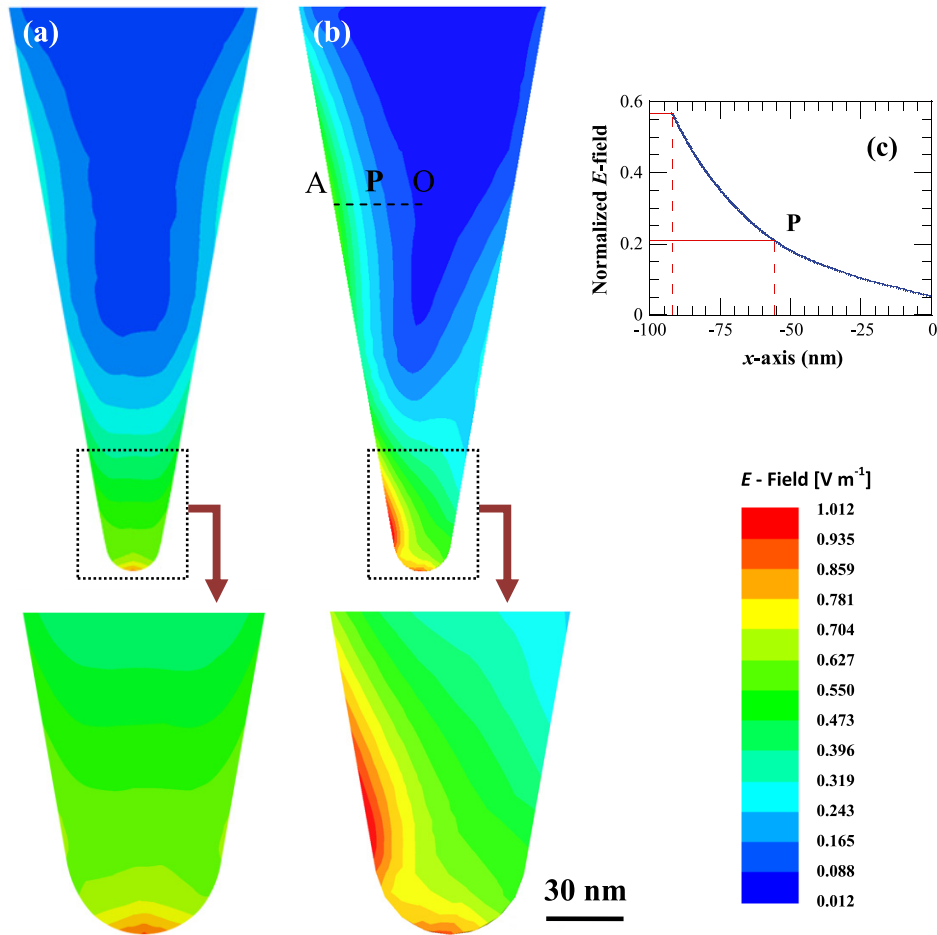


Figure 4. Electric field distribution inside the tip for (a) a front view of the y - z cross-section and (b) a side view of the x - z cross-section, and (c) along line AO. In figure (c) P is the point where the amplitude of electric field drops to e^{-1} of that on the surface, and AP is called the skin depth. The simulation conditions are the same as those for figure 2.

conclusions have been reported by Zayats [64], Downes [21], and Wang *et al* [35]. In figure 5, data for the relationship between field enhancement around the apex and polarization direction are depicted by circles. Obviously, the field enhancement declines as the polarization direction angle ϕ increases. When $\phi > 85^\circ$, no field enhancement under the tip apex exists (i.e. the enhancement factor is less than one). This is consistent with the results reported that incident light with polarization perpendicular to the tip axis results in no field enhancement [27, 31, 63].

However, Royer [41] demonstrated that for the component parallel to the tip axis the enhancement factor is about ten times larger than that obtained for the component perpendicular to the tip axis. If only taking into account the projection of the incident electric field on the z -axis, i.e. z -component, then the modified field enhancement, which is equal to the ratio of electric field intensity under the tip apex to the z -component of the incident electric field $E/E_{z,in}$, is independent of the polarization direction. This is clearly depicted by triangles in figure 5: a flat line appears as ϕ varies. So it is conclusive that the field enhancement depends on $\cos \phi$, and the perpendicular component of the incident electric field has no contribution to the field enhancement. Similarly, the intensity enhancement depends on the square of $\cos \phi$.

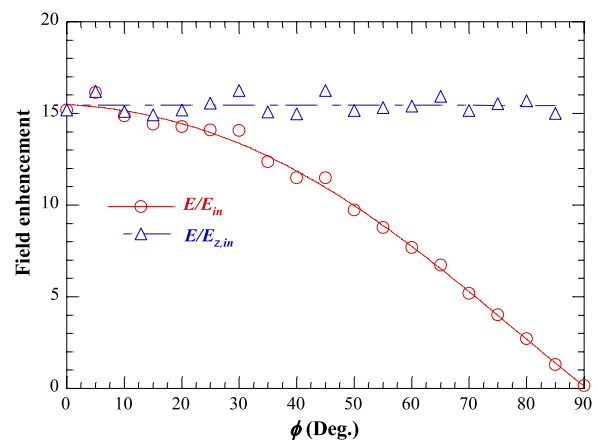


Figure 5. Field enhancement for different polarization angles. In these cases, $d = 5$ nm, $r = 30$ nm, and $\theta = 10^\circ$.

3.3. Effect of tip geometry

Since the tip and substrate are coupled, the tip-substrate distance has substantial influence on the performance of the system, like the atomic force and tunneling current being phenomenally sensitive to the tip-substrate distance in SPM

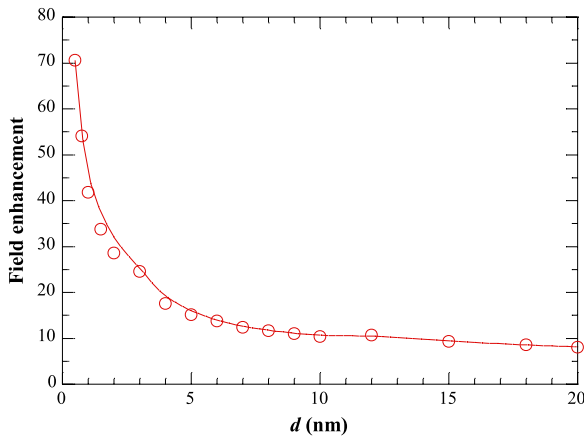


Figure 6. Dependence of the field enhancement on tip-substrate distance. In these cases, $\theta = 10^\circ$, $r = 30$ nm, and $\phi = 0^\circ$.

systems. Also, the resonant situation is strongly dependent on the tip-substrate distance. Demming *et al* figured out an inversely proportional relationship between field enhancement and the tip-substrate separation distance [30]. Madrazo *et al* also demonstrated a monotonic increase behavior as the tungsten probe approaches the interface [65]. In figure 6 we study the influence of the tip-substrate distance on the field enhancement. For $r = 30$ nm and polarization in the z direction when $d = 0.5$ nm, extremely strong field gradient is observed beneath the tip apex, where the field enhancement is as high as 71.6. As the tip-substrate distance increases, the field enhancement factor declines exponentially; when the distance reaches 5 nm, the field enhancement dramatically drops to 15.2. When $d > 5$ nm, the field enhancement decreases mildly. With $d = 20$ nm, field enhancement is only 8.1. As $d = \infty$, i.e. there is no substrate under the tip, the field enhancement factor is as low as 3.7.

Another interesting phenomenon is that the peak electric field position has a shift away from the tip axis surface on the tip surface as the tip-substrate distance increases, and similar results have been reported by Wang *et al*, who found that a field peak shift away from the tip axis was observed at large laser incidence angles [35]. Figure 7 shows the electric field distributions along the intersection line of the tip apex surface and x - z plane for different tip-substrate distances. When $d \leq 5$ nm, the peak position appears normally under the tip axis; the more the tip approaches the substrate, the more symmetrical the field appears on both sides of the tip apex along the x direction. When $d > 5$ nm, the peak position shifts away with a small distance (15–30 nm for these specific simulations) from the tip axis in the $+x$ direction (away from the laser incident direction); meanwhile, the field magnitude on the right of the tip axis is much larger than that on the left. If this phenomenon has been detected during laser-assisted nanopatterning experiments, the nanopattern under the tip also would be offset by a distance of 15–30 nm. Further experimental proof is needed of such phenomenon.

Figure 8 shows the field enhancement under the tip apex for various radii and half taper angles. The effects of tip radius on the field enhancement are present in figure 8(a) for $\theta = 10^\circ$,

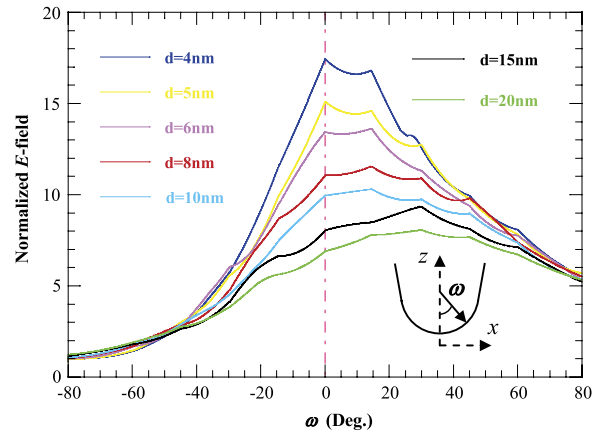


Figure 7. Electric field distribution along the tip surface in the x - z plane for different tip-substrate distances. For these simulations, $\theta = 10^\circ$, $r = 30$ nm, $\phi = 0^\circ$, are used.

$d = 5$ nm, and $\phi = 0^\circ$. When the apex radius increases from 5 to 9 nm, the field enhancement goes up from 15.3 to 17.2. When $r > 9$ nm, the field enhancement declines almost linearly with the increasing apex radius. The relationship between half taper angle and field enhancement is shown in figure 8(b). As the half taper angle θ increases from 0° to 25° , the field enhancement under the apex increases from 14.2 to 20.0. After 25° , the peak field enhancement experiences a plateau until $\theta = 35^\circ$.

4. Tip heating by the incident laser

4.1. Laser heating mechanism

In electromagnetic waves, the energy flow is described by the Poynting vector:

$$\mathbf{S} = \mathbf{E} \times \mathbf{H}, \quad (1)$$

where $\mathbf{E}(\mathbf{H})$ represents electric (magnetic) field. Substituting \mathbf{H} into \mathbf{E} according to Maxwell's equations, the Poynting vector gives the intensity (i.e. energy flow per unit area in W m^{-2}) of the incident light [66],

$$I = S = 0.5c\epsilon_0 n E^2, \quad (2)$$

where I is the intensity of incident light in W m^{-2} , c ($3 \times 10^8 \text{ m s}^{-1}$) is the light speed in free space, ϵ_0 is vacuum permittivity, n the refractive index of the medium. The heat generation rate per unit volume is $\dot{q} = I\alpha$, where $\alpha = 4\pi k/\lambda$ is termed the absorption coefficient, k is the extinction coefficient, and λ is the wavelength in free space.

The incident laser beam is assumed to be spatially uniform, corresponding to a plane wave in HFSS simulation, and has a temporal distribution as

$$I = I_0 \exp\left(-\frac{(t - t_0)^2}{t_g^2}\right), \quad (3)$$

where I_0 is a laser beam intensity constant, t_0 the peak time ($=20$ ns), and t_g ($=6$ ns) is a time constant. The profile of

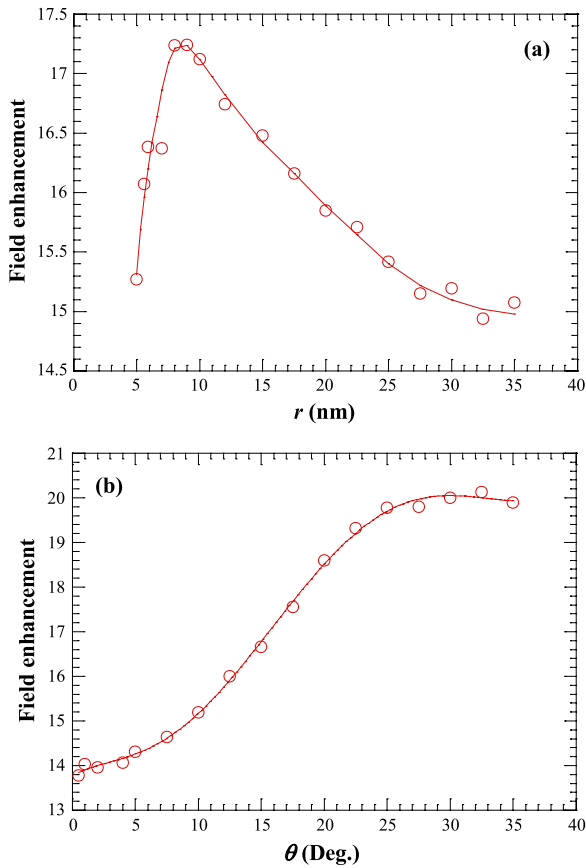


Figure 8. The effect of (a) apex radius and (b) half taper angle on field enhancement. Simulation conditions are (a) $\theta = 10^\circ$, $d = 5$ nm, $\phi = 0^\circ$, and (b) $r = 30$ nm, $d = 5$ nm, $\phi = 0^\circ$, respectively.

incident laser intensity is shown in figure 9. The full-width at half-maximum (FWHM) of the laser pulse is 10 ns centered at $t = 20$ ns. In our work, only a single laser pulse is considered, i.e. the total simulation time is 40 ns. In order to simplify the simulation, the pulse energy per unit area of the pulse q'' is set prudently to induce a moderate tip temperature rise less than 50 K. Consequently, the tip (tungsten) thermal conductivity and specific heat variation against temperature is less than 5%, and this small change can be neglected. Meanwhile, the reflectance, permittivity, and electric conductivity of tungsten can also be taken as constant, assuring we can use the field distribution inside the tip calculated at 300 K under other temperatures without causing too much variation.

In our study, the pulse energy per unit area of the incident laser is written as q'' , from which I_0 in equation (3) can be obtained. The intensity $I(t)$ of the incident laser at time t is calculated according to equation (3). Then we substitute $I(t)$ into equation (2) to obtain the incident electric field magnitude $E_{\text{inc}}(t)$ in vacuum. Since the electric field distribution inside the tip has been calculated in the former sections with unity incident electric field intensity, and obviously the linear relationship is valid between the incident electric field and the one inside the tip. The electric field distribution within the tip, $E_{\text{tip}}(x, y, z, t)$, under the condition that the energy density of the incident laser pulse is q'' can be obtained by scaling the previous calculated results. With $E_{\text{tip}}(x, y, z, t)$

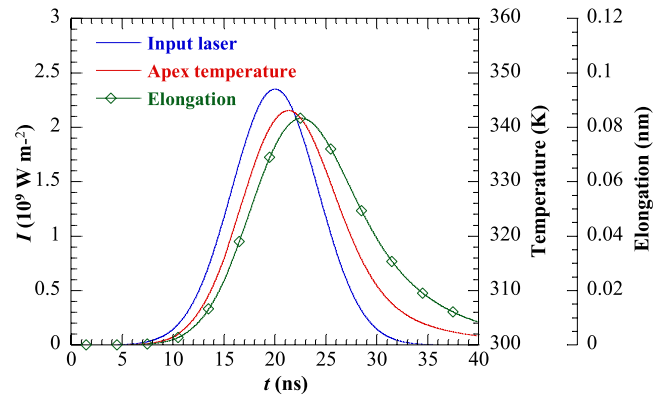


Figure 9. The incident laser pulse profile, tip apex temperature, and tip elongation over time under the illumination of the incident laser. The peak temperature, which is 343.08 K, is behind the peak of the laser pulse by 1.3 ns, and the largest elongation, 0.83 nm, is lagging 2.6 ns behind. Simulation conditions: $\theta = 10^\circ$, $r = 30$ nm, $d = 5$ nm, $\phi = 0^\circ$, and $q'' = 2.5$ mJ cm $^{-2}$.

and equations (2) and (3), the laser intensity absorbed in the tip $I_{\text{tip}}(x, y, z, t)$ as well as the heat generation rate per unit volume $\dot{q}_{\text{tip}}(x, y, z, t)$, which acts as a heat source inside the tungsten tip, can be calculated.

With the knowledge of heat source distribution within the tip, the temperature distribution would be available. Commercial computational software ANSYS FLUENT (V12.0.1 Ansys, Inc.) is used to simulate the temperature distribution within the tip. The length of the tip is 2 μ m, and the heat source is distributed at the small end of the 600 nm length following the laser illumination situation calculated by HFSS. Since the heat transmitted through the surrounding air by convection and heat transferred by radiation to the environment can be neglected for high thermal conductivity materials (the thermal conductivity of tungsten is 174 W m $^{-1}$ K $^{-1}$ at 300 K), it is reasonable to set the peripheral and hemispherical end surface as adiabatic. The large top end surface of the tip is set at 300 K. The initial temperature of the tip is 300 K.

4.2. Temperature evolution and distribution inside the tip

According to all our simulations, the highest temperature point is located at the tip apex during the laser illumination. Hence, the apex temperature can be used as a parameter for monitoring during simulation and for comparison. In this study, the incident laser energy is set to 2.5 mJ cm $^{-2}$. Figure 9 shows the incident laser intensity profile and the development of apex temperature over time under illumination from the incident laser. Because the heat conduction in the tungsten tip is very quick due to its high thermal conductivity, the profile of the apex temperature is akin to the incident laser profile. The maximal temperature increase is 43.1 K, and appears 1.3 ns behind the laser pulse peak. Such a delay is induced by heat conduction in the tip.

In figure 10 four x - z cross-sectional views of temperature distribution at different times are shown. In figure 10(a), $t = 10$ ns, only a third of the sharp end has been influenced by the incident laser heating, and the temperature distribution

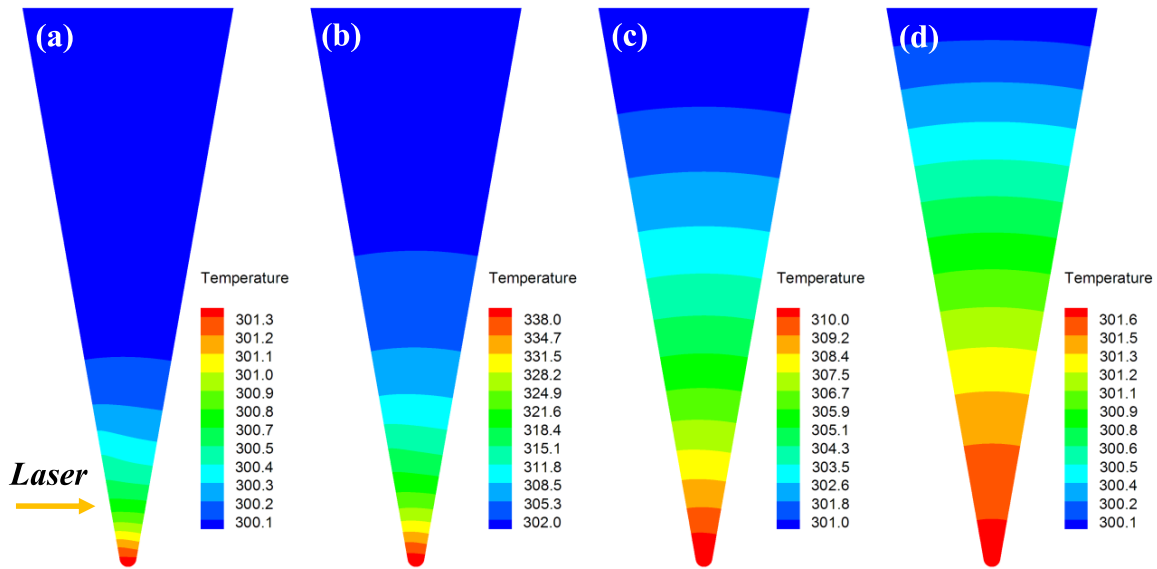


Figure 10. x - z cross-sectional view of the temperature distribution at (a) $t = 10$ ns, (b) $t = 20$ ns, (c) $t = 30$ ns, and (d) $t = 40$ ns. The simulation conditions are the same as those in figure 9.

is noticeably asymmetric to the tip axis. The temperature is higher in the front or laser incident side. The non-uniform temperature distribution would induce asymmetrical expansion, which has been confirmed in simulation results [37] and observed in experiments [67]. At 20 ns, the temperature gradient develops far away from the tip apex, and asymmetric temperature distribution still exists to some extent. At 30 ns, the temperature distribution is more evenly distributed along the tip axis direction; asymmetry only exists at the sharp end. At the end of laser heating (40 ns), the temperature distribution is fully developed, and asymmetry disappears. If the whole tip is divided into numerous concentric layers, or spherical crowns, as demonstrated in figure 1(b), it is obvious that each concentric spherical crown can be approximately treated as an isothermal layer, which is the same as in [37, 54] during the cooling process, especially for the zone far away from tip apex or for fully developed temperature. Furthermore, the temperature in the axis is used to represent the temperature of the corresponding concentric spherical crown. Consequently, the temperature distribution along the tip axis can fundamentally reflect the temperature distribution within the whole tip.

Thermal expansion of SPM tips induced by lateral laser heating has been reported in many works [11, 13, 35, 51, 52, 65, 66]. Thermal expansion from less than 0.01 nm [53], several nanometers [11, 54], and to as long as 15 nm has been observed [68]. As the thermal expansion of the tip is not the focus of this work, we only do the analysis for one heating condition to look into the physical behavior of the tip. Neglecting the weak non-uniformity of the temperature distribution in the tip radial direction, the tip elongation (δL) can be calculated as $\delta L = \int_0^L \alpha(T - T_0) dl$. T_0 is the initial temperature and α the linear thermal expansion coefficient of the tip ($4.5 \times 10^{-6} \text{ K}^{-1}$ for tungsten). The thermal elongation is calculated and shown in figure 9. The largest thermal

elongation is 0.83 nm, and is 2.6 ns behind the peak of the input laser pulse, or 1.3 ns behind the peak apex temperature. Thermal expansion delay was also reported in pulsed laser illumination [37]. Generally speaking, the thermal expansion is directly related to the temperature distribution along the tip axis, and it is in phase with the integrated temperature increase along the tip axis. The latter, as expected, is lagging in phase to the tip apex temperature. Comparing the three curves in figure 9, though the temperature and thermal elongation are lagging in phase with respect to the input laser, their responses are still quick enough to follow the change of the input laser in one pulse. This quick time response of the thermal expansion differs from that reported by La Rosa *et al* [47]. In their work, the tip is irradiated with a relatively long laser pulse (10^{-3} s or longer), and the tip thermal expansion features a two-time-constant behavior. The short time (initial) behavior reflects the quick thermal energy accumulation near the tip apex region, and the long time behavior is largely attributed to the thermal transport along the tip.

The temperature distribution profiles along the tip axis at different times during laser heating are shown in figure 11. The z -axis presents the distance to the tip apex. The lines with filled symbols represent the temperature increasing process or heating process, while all the other lines describe the temperature dropping process or cooling process. It is noted that the temperature changes dramatically at the sharp end, and mildly at the blunt end for all the lines. Additionally, the temperature in the blunt end lags behind that in the sharp end. After $t = 30$ ns, the temperature profiles are almost linear, corresponding to the homogeneous distributed color bands in figures 10(c) and (d).

4.3. Effect of laser polarization and tip geometry on heating

In order to investigate the laser absorption within the tip, the mean laser intensity enhancement (the square of the field

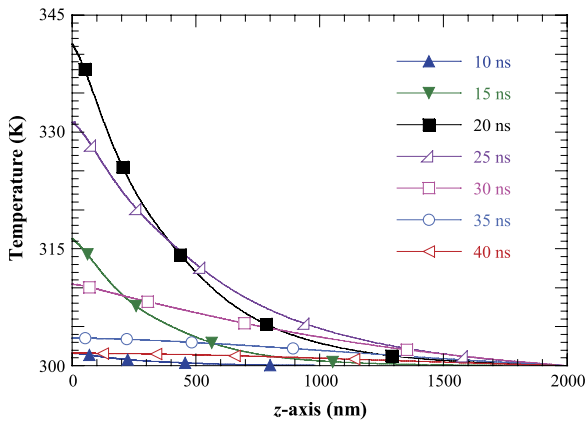


Figure 11. Temperature distribution along the axis of the tip at different times during laser heating. The z -axis is the distance to the tip apex. The simulation conditions are the same as those in figure 9.

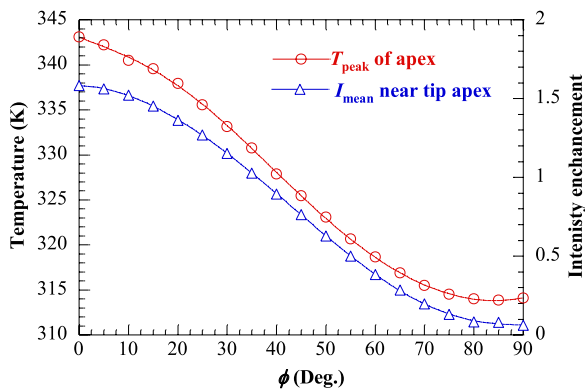


Figure 12. Peak apex temperature and mean laser intensity near the apex inside the tip versus polarization angles. Simulation conditions: $\theta = 10^\circ$, $r = 30$ nm, $d = 5$ nm, and $q'' = 2.5$ mJ cm $^{-2}$.

enhancement multiplying ratio of the refractive indices of tungsten and air) is observed in the process of simulation. Since the temperature of the tip apex is directly influenced by the heat source in the apex zone, which in turn is determined by the laser intensity, the mean laser intensity near the tip apex is extracted to correlate with the peak apex temperature. The decline in peak apex temperature and mean laser intensity near the tip apex versus polarization direction angle is shown in figure 12. In this study, the incident laser energy is chosen at 2.5 mJ cm $^{-2}$. As the ϕ increases, the laser intensity near the tip apex goes down gradually, which means the heat source declines with the increasing ϕ , which directly affects the peak apex temperature. The electric field or laser intensity within the tip also has the same dependence trend on polarization direction as the peak enhancement factors beneath the apex, as discussed in section 3.2. The mean laser intensity goes down as the polarization angle θ increases. This directly results in the peak apex temperature monotonously descending as θ becomes larger.

Besides the heat source, another factor which would affect temperature distribution within tips is the geometrical shape. The tip geometry directly determines its thermal resistance. For the tip, its thermal resistance R_t can be

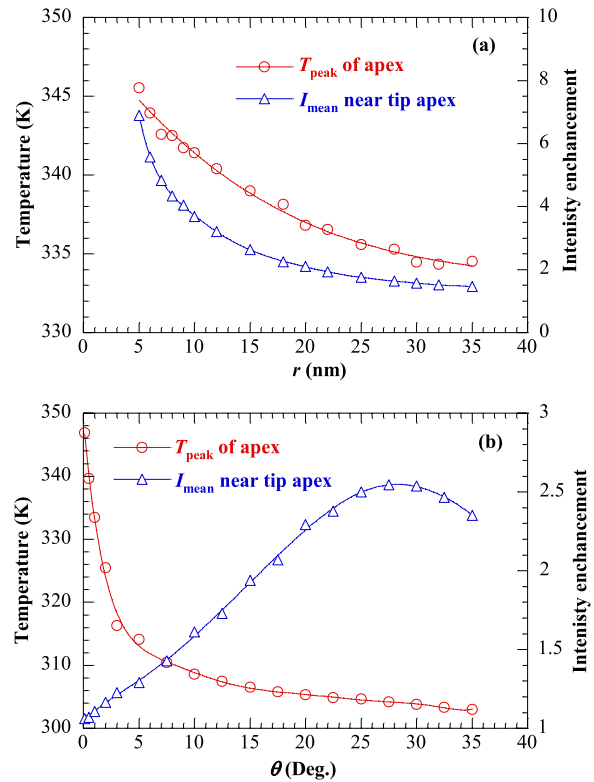


Figure 13. Peak temperature of the apex and mean laser intensity near the apex inside the tip versus (a) the apex radius and (b) the half taper angle. Simulation conditions: (a) $\theta = 10^\circ$, $d = 5$ nm, $\phi = 0^\circ$, and $q'' = 2.0$ mJ cm $^{-2}$; (b) $r = 30$ nm, $d = 5$ nm, $\phi = 0^\circ$, and $q'' = 0.5$ mJ cm $^{-2}$.

expressed approximately as (neglecting the apex region) $\sin \theta [1/r - 1/(r + L \sin \theta)] / [2\pi k(1 - \cos \theta)]$ or $[1/r - 1/(r + L \sin \theta)] / [2\pi k \tan(\theta/2)]$. It is easy to verify that the derivative of R_t on r is negative. Consequently, the thermal resistance decreases monotonically with the increasing tip radius r . Considering the fact that $1/r \gg 1/(r + L \tan \theta)$, it is obvious that when the half taper angle becomes larger, the thermal resistance will go down quickly.

The dependences of peak apex temperature on the apex radius and half taper angle are shown in figures 13(a) and (b) for incident laser pulse energy of 2.0 mJ cm $^{-2}$ and 0.5 mJ cm $^{-2}$, respectively. The laser intensity enhancement near the tip apex is also depicted. As r increases, the thermal resistance decreases, so heat is more easily dissipated in the radial direction, meanwhile, the laser intensity near the tip apex declines monotonously; both these factors would reduce the peak apex temperature, as presented in (a). In figure 13(b), for $r = 30$ nm, the peak apex temperature decreases as the half taper angle increases from 0° to 35° , which is similar to the results reported for aluminum-coated fiber tips [44, 48]. However, the mean laser intensity features a different trend: it increases almost with θ linearly until $\theta = 25^\circ$, then remains constant, only slightly declining when $\theta > 30^\circ$. When $\theta < 5^\circ$, the half taper angle is the dominating factor that influences the temperature inside the tip, explaining why the peak apex temperature drops abruptly down from 347.9 to 314.1 K even though the mean laser intensity near the tip apex

increases. As θ increases from 5° to 25° , the peak temperature decreases mildly due to compensation of the increasing mean laser intensity near the tip apex. As θ increases further, similar to the phenomenon in figure 13(a), both peak apex temperature and mean laser intensity near the tip apex decrease. Another factor which cannot be ignored is the surface-area-to-volume ratio, γ , where the surface area is the projection area along the laser propagation direction. Since the laser energy is absorbed on the tip surface and propagates toward the core, the larger γ , the higher the temperature the tip would reach. For the conical tip, γ is approximately $3/\pi(2\eta + L)/(3\eta^2 + 3\eta L + L^2)$, where $\eta = r/\sin\theta$. The derivative of γ with respect to η is negative. When r increases, η will increase and γ will decrease. The decline of the peak apex temperature against the tip radius is the combined effect of γ , heat source, and thermal resistance, as shown in figure 13(a). On the other hand, when θ increases, η decreases, and γ will increase. As a result, the temperature decline is offset somehow by the effect of γ and heat source, as shown in figure 13(b).

In order to analyze the thermal effect of the substrate on the tip, the thermal contact resistance between them needs to be calculated. Take the tungsten tip with $r = 30$ nm, $\theta = 10^\circ$, and $L = 16$ μm (typical length for commercial tip) for example; its thermal resistance is $R_{\text{tip}} = 3.452 \times 10^5$ K W $^{-1}$. In general, the thermal resistance (per unit area) between hard interfaces in simple mechanical contact is of the order of 10^{-5} m 2 K W $^{-1}$ or higher. Therefore the thermal contact resistance between the tip and the substrate is estimated to be 10^{11} K W $^{-1}$ if the tip is assumed to have a flat top of 10 nm diameter. The real value could be even larger. This very high thermal contact resistance allows very little heat transfer between the tip and the substrate under vacuum conditions. Therefore, the temperature distribution and evolution in the tip reported in this work does not consider the heat transfer effect of the substrate.

In our modeling, the tip radius is small, from 35 nm down to 5 nm. For tungsten at 300 K, its thermal conductivity is 174 W m $^{-1}$ K $^{-1}$, which is mostly contributed by electrons. Using approximated electron specific heat of the order of 2.1×10^4 J m $^{-3}$ K $^{-1}$ and electron speed $\sim 10^4$ m s $^{-1}$, and considering the strong energy exchange between electrons and lattice, the appearing mean free path of free electrons in tungsten is about 20 nm. Since the tip apex radius is smaller or comparable to this mean free path, it is expected in the apex region that the thermal conductivity of tungsten will be reduced accordingly. In the tip apex region, the characteristic thermal transport time (t_c) in the direction normal to the tip apex can be approximated as r^2/α where r is the tip radius and α is thermal diffusivity (6.83×10^{-5} m 2 s $^{-1}$ for bulk tungsten at 300 K). For a tip of 30 nm radius, the thermal conductivity in the tip region will have moderate reduction, and t_c is less than 1 ns. For smaller tips, even the thermal conductivity reduction is larger; considering the tip size has a second-order effect on t_c , the local t_c will be even smaller. This explains why there is very little temperature gradient in the tip apex region, as shown in figure 10. Therefore, the thermal conductivity reduction in the tip apex region has negligible effect on the thermal transport studied in this work. On the other hand, situations will change if the tip is under ultrafast laser (picosecond or femtosecond)

irradiation where the laser heating time is comparable to or smaller than the characteristic thermal transport time in the tip region.

5. Conclusion

In this work, the electromagnetic field was simulated in a tungsten SPM tip and silicon substrate system under laser irradiation. The electric field distribution around the tip apex and inside the tips had been analyzed. When the laser interacts with the metal tip, it is bent around the tip and concentrated under the apex, where extremely high field enhancement appeared. Field enhancement is mainly determined by the geometry of the tip–substrate system as well as their electrodynamic properties. As the tip–substrate distance increased, the peak field enhancement decreased exponentially. A shift of field peak position away from the tip axis was observed. This phenomenon vanished as the tip approached the substrate. If the polarization direction of the laser is not parallel to the tip axis, only the component along the tip axis makes a contribution to the electric field enhancement under the tip apex. The optimum tip apex radius for field enhancement is about 9 nm when the half taper angle is 10° . For a tip with a fixed radius of 30 nm, field enhancement increased as the half taper angle increased but was less than 25° . For a half taper angle in the range of 25° – 30° , the field enhancement kept pretty much constant. It decreased when the half taper angle went beyond 35° . A small fraction of light had penetrated into the tip and dropped dramatically near the surface. The resulting temperature distribution was affected by two kinds of factors: the heat source due to laser absorption and the geometric shape of the tip. The peak apex temperature was used as a comparison parameter. As the polarization angle or apex radius increased, the peak apex temperature decreased. The peak apex temperature declined as the half taper angle increased, even though the heat source provider—laser intensity inside the tip increased, revealing the strong effect of the half taper angle on thermal transport.

Acknowledgments

Support of this work by the National Science Foundation (CBET-0932573 and CMMI-0926704) is gratefully acknowledged.

References

- [1] Lewis A, Isaacson M, Harootunian A and Murry A 1984 *Ultramicroscopy* **13** 227–31
- [2] Pohl D W, Denk W and Lanz M 1984 *Appl. Phys. Lett.* **44** 651–3
- [3] Zenhausern F, Martin Y and Wickramasinghe H K 1995 *Science* **269** 1083–5
- [4] Lahrech A, Bachelot R, Gleyzes P and Boccara A C 1996 *Opt. Lett.* **21** 1315–7
- [5] Knoll B and Keilmann F 1999 *Nature* **399** 134–7
- [6] Bek A, Vogelgesang R and Kern K 2006 *Rev. Sci. Instrum.* **77** 043703
- [7] Esteban R, Vogelgesang R and Kern K 2009 *Opt. Express* **17** 2518–29
- [8] Jersch J and Dickmann K 1996 *Appl. Phys. Lett.* **68** 868–70

- [9] Münzer H-J *et al* 2002 *Proc. SPIE* **4426** 180–3
- [10] Chimmalgi A, Choi T and Grigoropoulos C P 2002 *ASME Int. Mechanical Engineering Congr. & Exposition (New Orleans, LA)* pp 1–5
- [11] Chimmalgi A, Grigoropoulos C P and Komvopoulos K 2005 *J. Appl. Phys.* **97** 104319
- [12] Feng X and Wang X 2008 *Appl. Surf. Sci.* **254** 4201–10
- [13] Boneberg J, Münzer H-J, Tresp M, Ochmann M and Leiderer P 1998 *Appl. Phys. A* **67** 381–4
- [14] Malshe A P *et al* 2010 *CIRP Ann.-Manuf. Technol.* **59** 628–51
- [15] Fleischmann M, Hendra P J and McQuillan A J 1974 *Chem. Phys. Lett.* **26** 163–6
- [16] Jeanmaire D L and van Duyn R P 1977 *J. Electroanal. Chem.* **84** 1–20
- [17] Campion A and Kambhampati P 1998 *Chem. Soc. Rev.* **27** 241–50
- [18] Kneipp K 2007 *Phys. Today* **60** 40–6
- [19] Anderson M S 2000 *Appl. Phys. Lett.* **76** 3130–2
- [20] Bailo E and Deckert V 2008 *Chem. Soc. Rev.* **37** 921–30
- [21] Downes A, Salter D and Elfick A 2006 *J. Phys. Chem. B* **110** 6692–8
- [22] Geshev P I, Fischer U and Fuchs H 2010 *Phys. Rev. B* **81** 125441
- [23] Hallen H D, La Rosa A H and Jahncke C L 1995 *Phys. Status Solidi a* **152** 257–68
- [24] Jahncke C L, Paesler M A and Hallen H D 1995 *Appl. Phys. Lett.* **67** 2483–5
- [25] Zeisel D, Deckert V, Zenobi R and Vo-dinh T 1998 *Chem. Phys. Lett.* **283** 381–5
- [26] Born M and Wolf E 1999 *Principles of Optics: Electromagnetic Theory of Propagation, Interference and Diffraction of Light* 7th edn (Cambridge: Cambridge University Press)
- [27] Novotny L, Bian R X and Xie X S 1997 *Phys. Rev. Lett.* **79** 645–8
- [28] Martin O J F and Paulus M 2002 *J. Microsc.* **205** 147–52
- [29] Lu Y-F, Mai Z-H and Chim W-K 1999 *Japan. J. Appl. Phys.* **38** 5910–5
- [30] Demming F, Jersch J, Dickmann K and Geshev P I 1998 *Appl. Phys. B* **66** 593–8
- [31] Martin O J F and Girard C 1997 *Appl. Phys. Lett.* **70** 705–7
- [32] Martin O J F, Girard C and Dereux A 1995 *Phys. Rev. Lett.* **74** 526–9
- [33] Krug J T II, Sánchez E J and Xie X S 2002 *J. Chem. Phys.* **116** 10895–901
- [34] Downes A, Salter D and Elfick A 2006 *Opt. Express* **14** 5216–22
- [35] Wang Z B, Luk'yanchuk B S, Li L, Crouse P L, Liu Z, Dearden G and Watkins K G 2007 *Appl. Phys. A* **89** 363–8
- [36] Sajanlal P R, Subramaniam C, Sasanpour P, Rashidianbc B and Pradeep T 2010 *J. Mater. Chem.* **20** 2108–13
- [37] Gerstner V, Thon A and Pfeiffer W 2000 *J. Appl. Phys.* **87** 2574–80
- [38] Jin J M 2002 *The Finite Element Method in Electromagnetics* 2nd edn (New York: Wiley-IEEE Press)
- [39] Micic M, Klymyshyn N, Suh Y D and Lu H P 2003 *J. Phys. Chem. B* **107** 1574–84
- [40] Shi J, Lu Y, Cherukuri R S, Mendu K K, Doerr D W, Alexander D R, Li L P and Chen X Y 2004 *Appl. Phys. Lett.* **85** 1009–11
- [41] Royer P, Barchiesi D, Lerondel G and Bachelot R 2004 *Phil. Trans. R. Soc. A* **362** 821–42
- [42] Zhang W, Cui X and Martin O J F 2009 *J. Raman Spectrosc.* **40** 1338–42
- [43] Kavaldjiev D I, Toledo-Crow R and Vaez-Iravanian M 1995 *Appl. Phys. Lett.* **67** 2771–3
- [44] Stähelin M, Bopp M A, Tarrach G, Meixner A J and Zschokke-Gränacher I 1996 *Appl. Phys. Lett.* **68** 2603–5
- [45] La Rosa A H, Jakobson B I and Hallen H D 1995 *Appl. Phys. Lett.* **67** 2597–9
- [46] Jakobson B I, La Rosa A, Hallen H D and Paesler M A 1996 *Ultramicroscopy* **61** 179–85
- [47] Lienau Ch, Richter A and Elsaesser T 1996 *Appl. Phys. Lett.* **69** 325–7
- [48] Kurpas V, Libenson M and Martsinovsky G 1995 *Ultramicroscopy* **61** 187–90
- [49] La Rosa A H, Biehler B and Sinharay A 2002 *Proc. SPIE* **4777** 420–3
- [50] Miskovsky N M, Park S H, Park H, He J and Cutler P H 1993 *J. Vac. Sci. Technol. B* **11** 366–70
- [51] Ukraintsev V A and Yates J T Jr 1996 *J. Appl. Phys.* **80** 2561–71
- [52] Depasse F, Gomès S, Trannoy N and Gossel P 1997 *J. Phys. D: Appl. Phys.* **30** 3279–85
- [53] Grafström S, Kowalski J, Numann R, Probst O and Wörtge M 1991 *J. Vac. Sci. Technol. B* **9** 568–72
- [54] Grafström S, Schuller P, Kowalski J and Neumann R 1998 *J. Appl. Phys.* **83** 3453–60
- [55] Geshev P I, Demming F, Jersch J and Dickmann K 2000 *Appl. Phys. B* **70** 91–7
- [56] Geshev P I, Demming F, Jersch J and Dickmann K 2000 *Thin Solid Films* **368** 156–62
- [57] Geshev P I, Klein S and Dickmann K 2003 *Appl. Phys. B* **76** 313–7
- [58] McCarthy B, Zhao Y, Grover R and Sarid D 2005 *Appl. Phys. Lett.* **86** 111914
- [59] Mai Z H, Lu Y F, Song W D and Chim W K 2000 *Appl. Surf. Sci.* **154/155** 360–4
- [60] Milner A A, Zhang K, Garmider V and Prior Y 2010 *Appl. Phys. A* **99** 1–8
- [61] Weaver J G and Frederikse H P R 2007 *CRC Handbook of Chemistry and Physics* Internet Version 87th edn, ed D R Lide (Boca Raton, FL: Taylor and Francis) pp 116–40, section 12
- [62] Roth R M, Panoiu N C, Adams M M, Osgood R M Jr, Neacsu C C and Raschke M B 2006 *Opt. Express* **14** 2921–31
- [63] Novotny L, Sánchez E J and Xie X S 1998 *Ultramicroscopy* **71** 21–9
- [64] Zayats A V 1999 *Opt. Commun.* **161** 156–62
- [65] Madrazo A, Nieto-Vesperinas M and García N 1996 *Phys. Rev. B* **53** 3654–7
- [66] Fox M 2006 *Quantum Optics: An Introduction* (London: Oxford University Press)
- [67] Jersch J, Demming F, Fedotov I and Dickmann K 1999 *Appl. Phys. A* **68** 637–41
- [68] Huber R, Koch M and Feldmann J 1998 *Appl. Phys. Lett.* **73** 2521–3